

SIMPLE: Simultaneous Multi-Plane Self-Supervised Learning for Isotropic MRI Restoration from Anisotropic Data

Rotem Benisty, Yevgenia Shteynman, Moshe Porat, Moti Freiman
 Technion – Israel Institute of Technology.
 Haifa, Israel.

be.rotem@campus.technion.ac.il

Anat Illivitzki
 Rambam Health Care Campus.
 Haifa, Israel.

Abstract

Magnetic resonance imaging (MRI) is crucial in diagnosing various abdominal conditions and anomalies. Traditional MRI scans often yield anisotropic data due to technical constraints, resulting in varying resolutions across spatial dimensions, which limits diagnostic accuracy and volumetric analysis. Super-resolution (SR) techniques aim to address these limitations by reconstructing isotropic high-resolution images from anisotropic data. However, current SR methods often rely on indirect mappings and limited training data, focusing mainly on two-dimensional improvements rather than achieving true three-dimensional isotropy. We introduce “SIMPLE,” a Simultaneous Multi-Plane Self-Supervised Learning approach for isotropic MRI restoration from anisotropic data. Our method leverages existing anisotropic clinical data acquired in different planes, bypassing the need for simulated downsampling processes. By considering the inherent three-dimensional nature of MRI data, SIMPLE ensures realistic isotropic data generation rather than solely improving through-plane slices. This approach’s flexibility allows it to be extended to multiple contrast types and acquisition methods commonly used in clinical settings. Our experiments show that SIMPLE outperforms state-of-the-art methods both quantitatively using the Kernel Inception Distance (KID) and semi-quantitatively through radiologist evaluations. The generated isotropic volume facilitates more accurate volumetric analysis and 3D reconstructions, promising significant improvements in clinical diagnostic capabilities. Our code base will be available upon acceptance.

1. Introduction

Magnetic resonance imaging (MRI) is a cornerstone in medical diagnostics, providing high-resolution images of soft tissues with unparalleled contrast. In abdominal imaging, MRI plays a crucial role in diagnosing and monitoring various abdominal conditions and anomalies such as liver cirrhosis, pancreatic tumors, and renal anomalies [5, 7, 9, 10, 18]. However, traditional MRI scans often produce anisotropic data, where the resolution differs across spatial dimensions, potentially limiting diagnostic accuracy and the ability to perform precise volumetric analysis [4, 21].

The anisotropy in MRI data arises primarily from the technical constraints and trade-offs inherent in the imaging process. Achieving high spatial resolution in MRI requires long acquisition times due to the need to sample a large number of spatial frequencies in k-space, the Fourier domain representation of the image [1]. In clinical settings, the time available for MRI scans is limited by patient comfort, motion artifacts, and the need for high throughput. In abdominal imaging, these constraints are further compounded by the challenges of capturing high-quality images of a region that is prone to motion artifacts from respiration and peristalsis. As a result, compromises are often made, leading to higher resolution in the in-plane dimensions (x and y) and lower resolution in the through-plane dimension (z).

To mitigate the effects of anisotropy and improve diagnostic accuracy, clinical practice often involves acquiring at least two volumes with high in-plane resolution, typically in axial and coronal planes [8]. This approach ensures that although one dimension may have a lower resolution in each individual volume, combining multiple orientations provides a more comprehensive and detailed view of anatomical structures. However, this method can still result

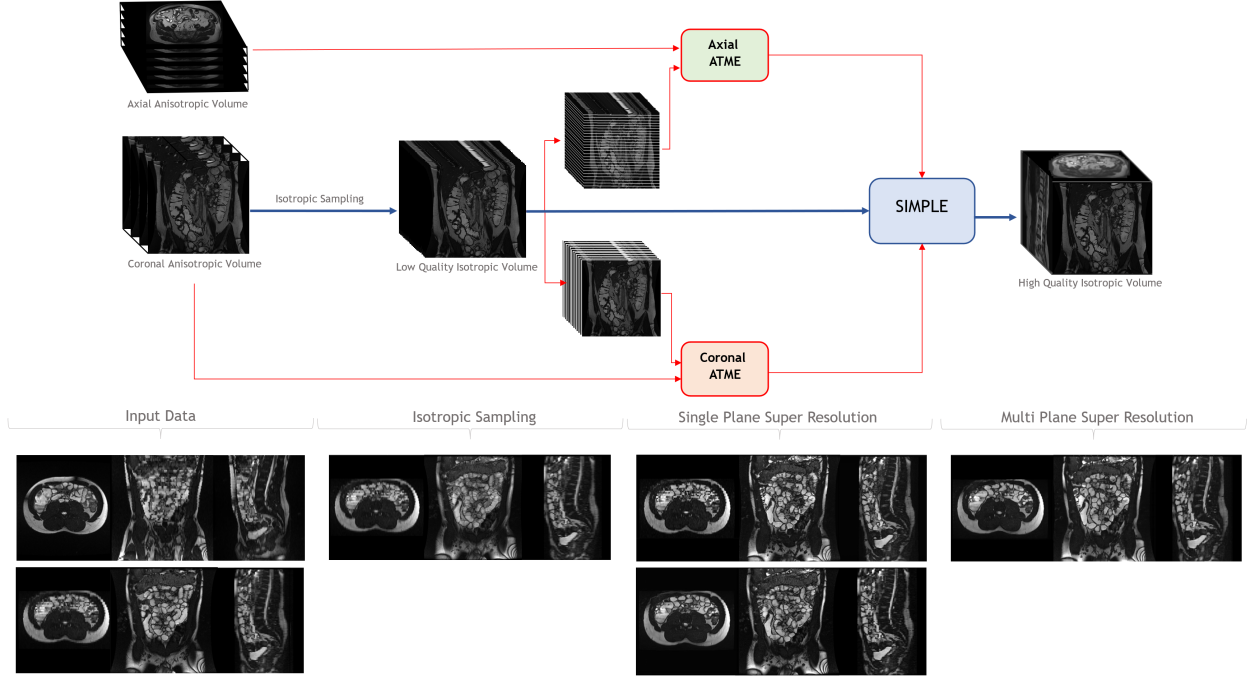


Figure 1. Our approach integrates ATME as a single-plane deep-learning-based super-resolution model [24] and employs a simultaneous multi-plane super-resolution model to achieve isotropic resolution. The red arrows represent components utilized exclusively during the training phase in the model architecture. In contrast, the blue arrow denotes the primary path of the model, used during both the training and inference phases.

in partial volume effects and diminished image quality, particularly in the slice-selection direction, leading to suboptimal volumetric analysis and 3D reconstructions. Furthermore, acquiring two planes increases the total scan time.

Super-resolution (SR) techniques have emerged as powerful tools to address these limitations, enabling the reconstruction of isotropic high-resolution images from anisotropic data [12]. These methods leverage advanced computational algorithms, often using neural networks, to learn a mapping from low-resolution (LR, with large inter-slice spacing) images to high-resolution (HR, with small inter-slice spacing) images. By enhancing the spatial resolution of MRI images, SR techniques facilitate better visualization of anatomical structures and pathological conditions, improve diagnostic performance, aid in surgical planning, and enhance the accuracy of quantitative assessments.

However, the abdomen poses unique challenges for MRI due to motion artifacts from respiration and peristalsis, and the need for high contrast between adjacent structures. Consequently, acquiring isotropic data for training purposes is not always feasible, particularly in clinical abdominal imaging. This limitation underscores the necessity for SR methods that can effectively work with the anisotropic data typically available in clinical settings.

In an effort to circumvent the need for real high-

resolution (HR) data for supervision, recent studies developed self-supervised methodologies, classified into resampling-based and synthesis-based techniques. Resampling-based techniques initially simulate images of even lower resolution from the original low-resolution (LR) images, establish a mapping from these lower-resolution images to the LR images, and subsequently apply this mapping to the LR images to forecast the HR images [13]. Synthesis-based techniques, on the other hand, synthesize HR images from the original LR images and train the super-resolution (SR) model on these synthesized images [16, 20, 27].

Despite their innovation, current self-supervised SR methodologies are hindered by limited training data and indirect mapping strategies. Notably, the training sets are derived from a limited number of LR cases, and the SR mapping is learned from lower-resolution to low-resolution data or from synthesized LR to synthesized HR data, as opposed to actual LR-HR pairs. This indirect mapping could significantly impede the performance of the model. Moreover, existing approaches primarily focus on interpolating the missing slices in the anisotropic volume, rather than simultaneously accounting for the inherent three-dimensional nature of the data.

In this work, we propose “SIMPLE,” a Simultane-

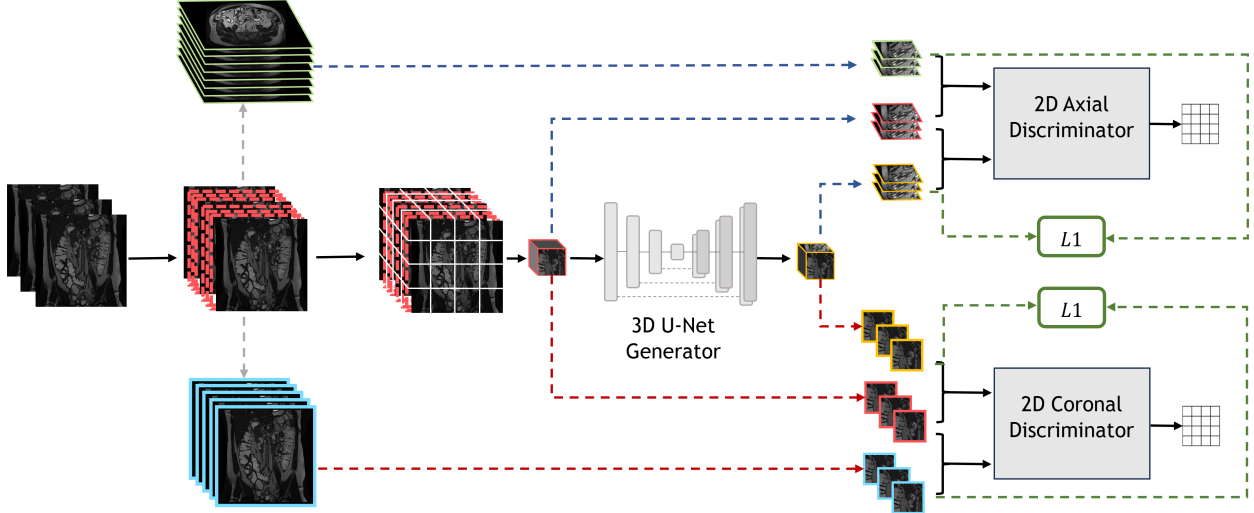


Figure 2. Model Architecture: The dashed red volume denotes the linearly interpolated volume. The blue-framed images represent the ATME-generated single-plane high-quality coronal slices, while the green-framed images represent the ATME-generated single-plane high-quality axial slices. The red dashed arrows indicate sampling along the coronal plane, and the blue dashed arrows indicate sampling along the axial plane. Gray dashed arrows depict the ATME flow, and green dashed arrows highlight the connections to consistency loss.

ous Multi-Plane Self-Supervised Learning approach for Isotropic MRI Restoration from Anisotropic Data. Our method leverages existing anisotropic clinical data acquired in different planes, avoiding the reliance on approximated simulated downsampling processes. Additionally, our approach considers the inherent three-dimensional nature of the data, rather than solely focusing on improving the quality of the two-dimensional slices in the through-plane direction. The flexibility of our approach in not requiring specialized data allows for seamless extension to multiple contrast types and acquisition methods commonly used in clinical practice. Figure 1 provides a comprehensive overview of our model architecture, including essential pre-processing steps such as linear interpolation and patch extraction. It also highlights the core components: the generator and two discriminators, which are crucial for ensuring simultaneous multi-plane realistic generation of the isotropic MRI volume.

Upon training, our approach efficiently produces a 3D isotropic MRI volume from a single anisotropic scan, alleviating issues related to inevitable abdominal motion between volumes and reducing the overall acquisition time required to obtain anisotropic volumes in two distinct planes. The generated isotropic volume ultimately facilitates more accurate volumetric analysis and 3D reconstructions.

2. Previous Work

The application of deep learning for through-plane super-resolution in MRI, which involves learning the non-linear mapping between low and high-resolution images,

has seen significant advancements in recent years. Early supervised learning approaches necessitated high-resolution training examples [17, 19, 25]. However, in clinical practice, acquiring such images is often impractical or even impossible, especially in the context of abdominal imaging. To address this limitation, several unsupervised methods have been proposed. Jog et al. [13] proposed an approach where the LR plane is first downsampled further, creating an LR^2 dataset. This dataset is then used to build $LR-LR^2$ image pairs, which are employed to learn the mapping from LR^2 to LR. Finally, this mapping is applied to the LR data to enhance its resolution.

Zhao et al. [27] used the high-resolution (HR) plane of the anisotropic volume to create HR-low-resolution (LR) image pairs by downsampling the HR plane for their “SMORE” model. The trained model is then applied to the LR plane to enhance its resolution. Remedios et al. [20] improved this by learning the point-spread-function (PSF) in the LR plane to more accurately simulate the down-sampling process in the HR plane, creating HR-LR image pairs for training. The trained model is then applied to two LR planes, with the restored volumes averaged into a single HR isotropic volume. Similarly, Lu et al. [16] proposed a Two-stage Self-supervised Cycle-consistency Network (TSCNet) for MR slice interpolation. This method uses a two-stage self-supervised learning (SSL) strategy. In the first stage, paired LR-HR images are synthesized along the sagittal and coronal directions of input LR images for network pretraining. In the second stage, a cyclic interpolation procedure based on triplet axial slices is designed for

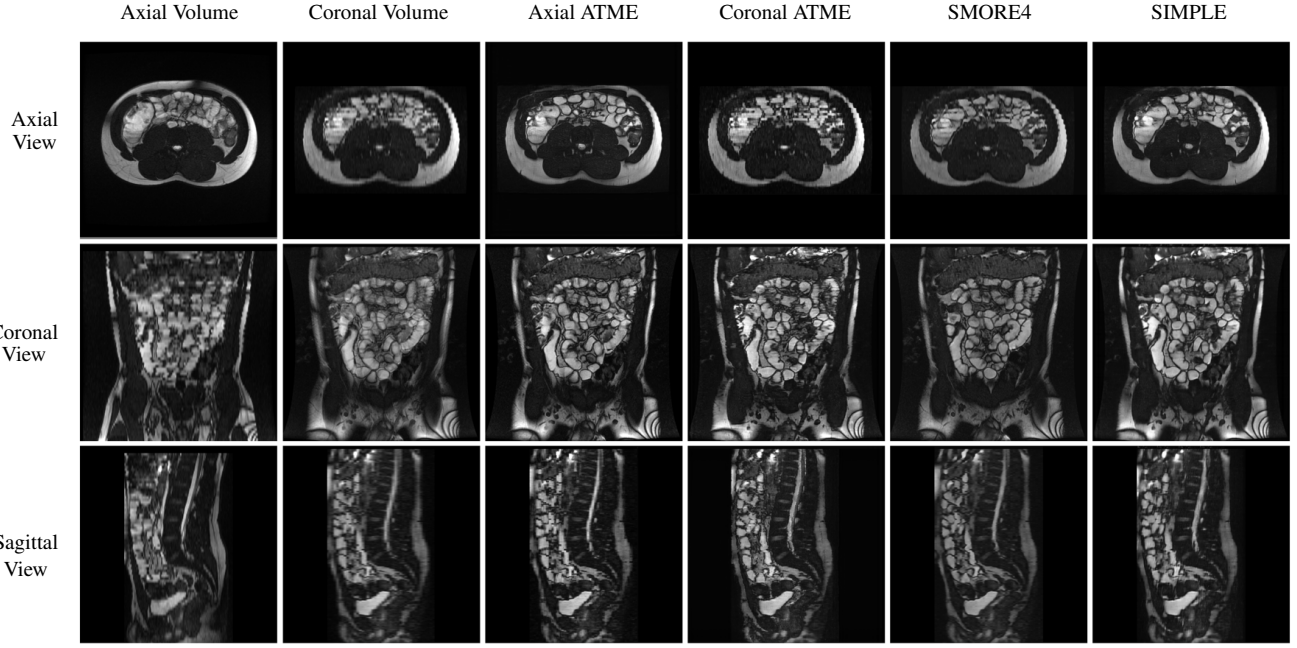


Figure 3. Multi-plane view of slices sampled from the isotropic MRI volume generated by SIMPLE in comparison to five competitive methods (from left to right): linear interpolation on anisotropic axial volume, linear interpolation on anisotropic coronal volume, ATME on anisotropic axial volume, ATME on anisotropic coronal volume, SMORE4 on anisotropic coronal volume, and SIMPLE on anisotropic coronal volume. Our approach, SIMPLE, produced higher-quality slices simultaneously on all planes compared to the other methods, which produced high-quality slices along the super-resolution plane but resulted in artifacts in the other planes.

further refinement.

Zhang et al. [26] used a similar approach to construct HR-LR image pairs for training and adapted the implicit neural representation (INR) network to implement a 2D arbitrary-scale super-resolution (SR) model. Recently, Fang et al. [6] introduced "CycleINR," an enhanced INR model for 3D volumetric super-resolution in medical data. They utilized the continuity of the implicit function for super-resolution at arbitrary up-sampling rates, eliminating the need for separate training. Additionally, they improved grid sampling with a local attention mechanism and reduced over-smoothing by incorporating a cycle-consistent loss.

Sander et al. [22] proposed an unsupervised deep learning semantic interpolation approach that synthesizes new intermediate slices from encoded low-resolution examples. They achieved semantically smooth interpolation in the through-plane direction by exploiting the latent space generated by autoencoders. New intermediate slices were generated by combining latent space encodings of two spatially adjacent slices using their convex combination. The combined encoding was then decoded into an intermediate slice.

However, these methods assume a high-quality approximation of the downsampling process and focus on generating high-resolution images in the through-plane, neglecting the three-dimensional isotropic nature of the data. In con-

trast, our approach uses existing anisotropic clinical data acquired in different planes, avoiding reliance on simulated downsampling. Our method accounts for the inherent 3D nature of the data, rather than solely improving the quality of 2D slices in the through-plane direction.

3. Method

To address the limitations of previous works and enable simultaneous multi-plane processing, we introduce SIMPLE—a simultaneous multi-plane self-supervised learning model for isotropic super-resolution MRI volume reconstruction from anisotropic MRI data acquired using 2D MRI techniques. Our model effectively manages slice spacing and motion, enhancing the resolution and quality of the 3D MRI volume. This improvement ensures that sampling along any plane (either axial or coronal) results in high-quality 2D slices in both planes. SIMPLE takes as input an anisotropic volume, and produces a low-quality isotropic volume using a linear interpolation. Then, the model restores a high-quality isotropic volume from the low-quality one. Equation 1 provides a mathematical framework for the proposed model. V_{Cor} denotes the anisotropic coronal volume, V'_{Iso} represents the linearly interpolated low-quality isotropic volume, \hat{V}_{Iso} signifies the output high-quality isotropic volume, GM denotes the generative model

and L the linear interpolation operator. This formulation distinguishes our approach by addressing both constraints, unlike previous methods which typically focus on resolving only one constraint.

$$\begin{aligned} \hat{V}_{\text{Iso}} &= GM(V'_{\text{Iso}}) = GM(L(V_{\text{Cor}})) \\ \text{s.t. :} \\ \text{I. } S_{\text{HR}_{\text{Cor}}} &= \hat{V}_{\text{Iso}}[i, :, :] = HR(V'_{\text{Iso}}[i, :, :]) \\ \text{II. } S_{\text{HR}_{\text{Ax}}} &= \hat{V}_{\text{Iso}}[:, i, :] = HR(V'_{\text{Iso}}[:, i, :]) \\ i &\in [0, 512] \end{aligned} \quad (1)$$

We implemented our approach by combining a 3D generator based on the U-Net architecture [3] with two 2D conditional patch discriminators [11], specifically designed for the coronal and axial planes. Figure 2 depicts the overall architecture.

3.1. Model Architecture

3.1.1 Pre-Processing

As a pre-processing step, we isotropically sample the anisotropic input volume by performing linear interpolation. Due to the significant spacing between the MRI slices, linear interpolation struggles to accurately predict the voxels between the slices, resulting in a low-quality 3D volume. This is reflected in the poor quality of slices in all main 2D planes. To manage the high computational demands of processing the uniform isotropic volume, we extracted 3D patches of size $64 \times 64 \times 64$ with an 8% overlap in each dimension.

3.1.2 Networks

We employ a 3D domain generator based on the 3D U-Net architecture [3] that takes a $64 \times 64 \times 64$ single-channel, low-quality 3D patch as input and outputs a high-quality patch of the same dimensions. This convolutional neural network has a contracting path for capturing context and an expanding path for precise localization, making it effective for tasks where feature location is critical. The encoder-decoder architecture includes skip connections: the encoder has multiple convolutional layers (kernel size 4, stride 2) with LeakyReLU activation and instance normalization, while the decoder uses transposed convolution layers (kernel size 4, stride 2) with ReLU activation, instance normalization, and dropout layers.

We use two discriminators: one for the coronal plane and another for the axial plane. Unlike the 3D generator, these discriminators operate in the 2D domain. We extract 3D input and output patches along both planes from the generator, creating 64 2D patches of size 64×64 from each 3D patch. Inspired by the pix2pix model [11], each plane has a conditional patch discriminator that takes the input image

and either the generated or real image as a single 2-channel input, ensuring the generated image remains realistic and consistent.

The patch discriminator focuses on local features and textures by dividing the image into patches and evaluating their authenticity independently. Real and synthetic samples are input as 2D patches with two channels: the first channel is a patch from the low-quality isotropic 3D input to the generator, and the second channel differs between real and synthetic samples. For synthetic samples, it is a 2D patch from the generator’s 3D output, while for real samples, it is a 2D patch from a high-resolution isotropic MRI volume in a specific plane.

Both discriminators use 2D convolutional layers (kernel size 4, stride 2), followed by instance normalization and LeakyReLU activation. Since the volume’s original orientation is in the coronal plane, the generator’s task is simpler in this orientation than in the axial plane. To increase complexity in the coronal plane, we use a simpler architecture for the coronal discriminator, with fewer layers and filters.

3.1.3 Loss Functions

For the SIMPLE generator, we employ a loss function that equally integrates both coronal and axial components. Each component comprises two types of loss: adversarial loss $\mathcal{L}_{\text{GADV}}$, derived from the discriminator’s output classification matrix, and consistency loss \mathcal{L}_{L1} , calculated as the L1 distance. For the discriminators, we use only the adversarial loss. The adversarial loss is based on a least square GAN (LSGAN), which provides more stable training compared to vanilla GANs, and conditional patch discriminator. Equation 2 represents the LSGAN loss for the generator, where x denotes the input image.

$$\mathcal{L}_{\text{GADV}} = \mathcal{L}_{\text{LSGAN}}(G, D) = \mathbb{E}_x [(D(x, G(x)) - 1)^2] \quad (2)$$

Equation 3 represents the LSGAN loss for the discriminator, where y denotes the ground truth image corresponding to the input image x .

$$\begin{aligned} \mathcal{L}_{\text{DADV}} = \mathcal{L}_{\text{LSGAN}}(D) &= \frac{1}{2} \mathbb{E}_{x,y} [(D(x, y) - 1)^2] + \\ &\quad \frac{1}{2} \mathbb{E}_x [(D(x, G(x)))^2] \end{aligned} \quad (3)$$

By incorporating consistency loss, the generator aims not only to deceive the discriminator but also to closely approximate the ground truth output. We choose L1 distance because it encourages sparsity and sharp edges in the generated image, effectively reducing blurring. Equation 4 represents the L1 distance metric between the generated 2D patches and the super-resolution 2D patches, with λ denoting the weight for this loss. We set λ to 10.

$$\mathcal{L}_{L1}(G) = \lambda \mathbb{E}_{x,y} [\|y - G(x)\|_1] \quad (4)$$

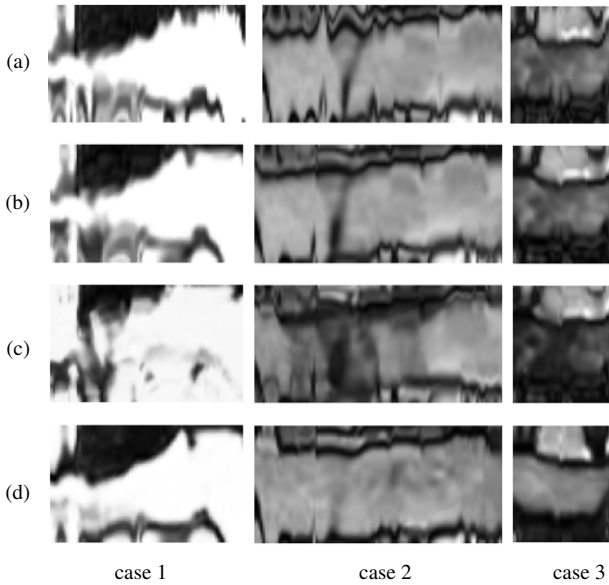


Figure 4. Straight multi-planar reconstructions (MPR) of the terminal ileum in Crohn’s disease patients for three cases based on coronal volumes: (a) anisotropic volume, (b) linearly interpolated isotropic volume, (c) SMORE4 isotropic volume, and (d) SIMPLE isotropic volume. The MPRs generated from the SIMPLE reconstructed volume were less prone to artifacts stemming from the anisotropic MRI acquisition.

Equation 5 represents our total generator loss:

$$\mathcal{L}_G = \alpha [\mathcal{L}_{G\text{ADV}_{\text{cor}}} + \lambda_{\text{cor}} \mathcal{L}_{L_{1\text{cor}}}] + \beta [\mathcal{L}_{G\text{ADV}_{\text{ax}}} + \lambda_{\text{ax}} \mathcal{L}_{L_{1\text{ax}}}] \quad (5)$$

where α and β denote the weights of the coronal and axial components, respectively. We set α and β both to 0.5.

3.2. Training

Figure 2 illustrates the training process step-by-step using the dashed red arrows. The key components of the training involve isotropic sampling, detailed in section 3.1.1, performing single-plane super-resolution on the axial and coronal planes as an initial step to generate paired data for the conditional model, and ultimately, training the generator and discriminators.

3.2.1 Single Plane Super Resolution

Although our database contains axial and coronal MRI sequences for each case, these sequences were scanned at different times. Consequently, the physiological motion of digestive tract organs (such as the bowel) and patient movement during scanning can cause shifts in the area within the field of view (FOV) of these sequences. This leads to motion artifacts and results in incomplete and inconsistent coverage of the patient anatomy between these two sequences. As a result, we cannot rely on these sequences

as ground truth for our model and must address the problem using an unsupervised method. However, to still provide real samples to our model, we perform a single image deep-learning-based super-resolution model on the interpolated isotropic low-resolution MRI volume for each plane separately. This approach yields two isotropic volumes, each with high resolution in only one plane. For the single-image super-resolution model, we choose ATME, a recent approach for image-to-image translation tasks that integrates elements from GAN and diffusion models [24]. We train two ATME models, each on a different plane, and evaluate them on slice samples from the interpolated isotropic volume in the coronal and axial planes.

3.2.2 Training Setup

The generator and the two discriminators are trained together for 100 epochs with a batch size of 16. The learning rate is initially set to 0.0002 and updated using a step scheduler. The Adam optimizer is employed to update the model parameters, with beta1 set to 0.5 and beta2 set to 0.999.

4. Experiments

4.1. Dataset

We obtained the appropriate Institutional Review Board (IRB) approval for retrospective data analysis. We collected 115 consecutive 2D MRI scans of Crohn’s Disease (CD) patients from a local hospital. All the MRI scans were acquired with a GE Medical Systems 3T MRI scanner. For the study, we utilize the coronal and axial FIESTA sequences. In both Coronal and Axial cases, the slice spacing and slice thickness are both set at 5mm, ensuring there is no overlap between adjacent slices. The average pixel spacing for the coronal sequences ranged from 0.7 mm to 0.94 mm in the x and y directions (mean 0.78 mm), while for the axial sequences, it ranged from 0.66 mm to 0.94 mm (mean 0.76 mm).

Since the number of slices varies for each case, the 3D size of the resulting isotropic volume differs accordingly. To standardize the isotropic volume to a uniform size of 512 in each dimension, we apply zero padding by adding empty slices along the edges of the coronal plane during the evaluation of our model.

4.2. Comparison Methods

We compare SIMPLE to linear interpolation and the SMORE4 [20] model using all performance metrics. All methods were trained and evaluated on the same coronal anisotropic MRI volumes.

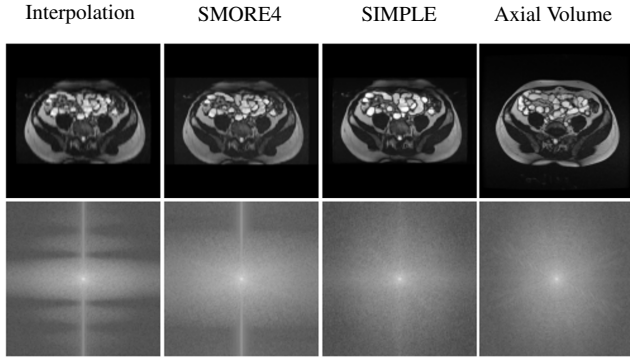


Figure 5. Fourier representation of axial slices generated from an anisotropic coronal volume. The Fourier representation of the axial slice produced by SIMPLE shows a more consistent distribution of the Fourier coefficients across the two dimensions of the image, whereas both the interpolated image (left) and the high-resolution SMORE4 image exhibit sampling artifacts. Compared to the closest slice from the axial volume (right), SIMPLE produces a similar Fourier representation, although it differs in the image domain due to the inconsistent field of view.

4.3. Qualitative Methods

We evaluate SIMPLE’s qualitative performance through visual assessment and senior radiologist feedback. Our methods include examining generated slices in three-plane views, performing straight multi-planar reconstructions of the small intestine, analyzing the Fourier domain, and obtaining Likert scale rankings for 10 cases from our dataset.

Multi View Slices:

We examine sampled slices in the coronal, axial, and sagittal planes for SIMPLE and five comparison methods, evaluated on coronal or axial anisotropic volumes. Due to the lack of 3D isotropic volumes in our dataset, we do not have ground truth slices for comparison.

Straight Multi Planar Reconstruction (MPR):

We use an in-house application to create straight multi-planar reconstructions (MPRs) [14] of the small intestine, allowing assessment of voxel correlations in the 3D domain. We utilized a dataset of Terminal Ileum (TI) centerlines from Crohn’s Disease (CD) patients, manually annotated by an attending radiologist on the same MRI database from our local hospital.

Fourier Domain:

To analyze the frequency components of the generated slices, we apply the Fourier transform to sampled axial slices from the generated isotropic volume. This evaluates

the preservation of high-frequency details, such as textures and edges, assessing the similarity between natural images and MRI images in the axial plane.

Likert Scale:

A senior radiologist ranked slices from 10 cases in our dataset across the coronal, axial, and sagittal views. These slices were sampled from isotropic volumes generated by SIMPLE, SMORE4, and linear interpolation. The radiologist, blinded to the methods used, assigned rankings on a Likert scale from 1 to 5: 1 for non-diagnostic images, 2 for poor quality, 3 for partial visualization of anatomy with blurry borders, 4 for good visualization with mild blurring, and 5 for excellent visualization.

4.4. Quantitative Methods

We quantitatively compared our method with SMORE4 and linear interpolation using distribution-based metrics: Kernel Inception Distance (KID) and Inception Score (IS) [2], derived from the InceptionV3 network. Additionally, we evaluated the Fréchet Inception Distance (FID) [15] using the VGG16 architecture [23] as the backbone. We computed FID on overlapping tiles of 96×96 pixels with a stride of 32 pixels. To reduce inaccuracies from linear interpolation, we selected slices approximating the midpoint between two original coronal slices. For the axial FID calculation, we chose axial slices whose physical locations are closest to the original axial sequence. This ensures that the generated axial distribution is compared to slices representing the same volume in physical space.

5. Results

5.1. Comparison of Ours to Baselines

Multi View Slices:

Figure 3 presents views of the three primary planes of isotropic MRI volumes generated by SIMPLE and five other methods. SIMPLE effectively enhances quality and resolution in both axial and coronal planes, unlike methods that favor a specific plane. Interpolation and ATME improve the plane quality corresponding to their original anisotropic acquisition. Both SIMPLE and SMORE4 improve resolution and quality across all planes but SIMPLE excels in the axial plane by better detecting and sharpening edges and improving contrast. In the coronal plane, the differences between SIMPLE and SMORE4 are subtle, with some organ locations differing. Additionally, SMORE4 is sensitive to organ shadows and emphasizes noise. Although SIMPLE has no constraints on the sagittal plane, it improves resolution similarly to SMORE4, which does have such constraints.

	Interpolation	SMORE4	SIMPLE
Axial	1	2.182 \pm 1.168	3.727 \pm 0.786
Coronal	1.231 \pm 0.438	4.231 \pm 0.438	4.615 \pm 0.65
Sagittal	1	1.5 \pm 0.527	2.2 \pm 0.789

Table 1. Average and standard deviation of the Likert scale ranking for all 3 main planes.

Straight Multi Planar Reconstruction (MPR):

Figure 4 depicts three straight MPRs based on four volumes: the original anisotropic volume and isotropic volumes generated by interpolation, SMORE4, and SIMPLE. SIMPLE’s reconstruction appears smoother compared to both the anisotropic and interpolated isotropic volumes, which contain discontinuities due to the larger gap between slices and inadequate generation. In some cases, the straight MPR of SMORE4 appears blurrier than that of SIMPLE.

Fourier Domain:

Figure 5 shows the Fourier domain of axial slices from isotropic volumes generated by interpolation, SMORE4, and SIMPLE models. SIMPLE’s Fourier transform resembles that of natural images, with a balanced mix of high and low frequencies. In contrast, the interpolated slices exhibit horizontal stripes due to the anisotropic resolution in the axial plane. Similarly, SMORE4 displays a prominent horizontal stripe near the center. All methods show distinct vertical and horizontal lines around the center, likely caused by zero-padding applied to the isotropic volume.

Likert Scale:

Table 1 presents the average and standard deviation of Likert scale rankings for each main plane across different methods: interpolation, SMORE4, and SIMPLE. As expected, linear interpolation received the lowest average rank. For the coronal plane, SMORE4 and SIMPLE achieved similar ranks, with SIMPLE having a slight advantage. In the axial plane, SIMPLE’s average rank is significantly higher than SMORE4’s. In the sagittal plane, both methods received low ranks, but SIMPLE’s rank is higher.

Distribution-Based Metrics:

Table 2 presents the metric scores for each of the three methods. For the coronal plane, SIMPLE scores lower than interpolation but higher than SMORE4 across all metrics. In the axial plane, SIMPLE achieves the lowest scores. Overall, SIMPLE has the lowest average scores for both planes. SMORE4 performs well in the coronal plane but struggles in the axial plane, resulting in a higher score ratio

	Interpolation		SMORE4		SIMPLE	
	Coronal	Axial	Coronal	Axial	Coronal	Axial
KID	3.829	48.185	0.894	40.554	2.383	32.487
	26.007		20.724			17.435
IS	0.031	0.023	0.001	0.033	0.003	0.006
	0.027		0.017			0.004
FID	17.292	28.964	14.897	23.938	16.834	21.316
	23.128		19.417			19.075

Table 2. Distribution-based metrics for sampled axial and coronal slices from the generated isotropic volume. It includes the scores for each plane individually, as well as the average score for both planes. Lower scores indicate better performance for all metrics.

Method	Mertic					
			KID		IS	
	Coronal	Axial	Coronal	Axial	Coronal	Axial
(a)	✓	-	0.268	39.597	0.0027	0.0219
			19.932			0.0123
(b)	-	✓	4.218	32.451	0.0031	0.0047
			18.334			0.0039
SIMPLE	✓	✓	2.383	32.487	0.0027	0.0058
			17.435			0.0042

Table 3. Ablation study results. The full SIMPLE model results compared to partial models based on a single coronal (a) or axial (b) discriminator.

between the planes compared to the more balanced ratio for SIMPLE.

5.2. Ablation Study

To evaluate the impact of individual design components in our model, we conducted two ablation studies, each testing the performance of a single discriminator. Table 3 presents the KID and IS scores for these models compared to our SIMPLE model. Model (a) achieves the lowest KID score in the coronal plane, while model (b) achieves a value similar to SIMPLE. For the IS metric, all models have similar coronal plane scores, with model (b) again close to SIMPLE. These results indicate that the axial discriminator contributes more than the coronal discriminator. This outcome was expected, as the input volume was acquired in the coronal plane, leading to a higher initial resolution in the coronal plane compared to the axial plane in the anisotropic volume. Yet, the combination of both discriminators in SIMPLE resulted in the smallest averaged KID distance reflecting the importance of the simultaneous optimization.

6. Conclusion

We introduce “SIMPLE,” a Simultaneous Multi-Plane Self-Supervised Learning approach for isotropic MRI restoration from anisotropic data. Our approach leverages anisotropic clinical data acquired in different planes, avoiding reliance on simulated downsampling. By considering the inherent three-dimensional nature of MRI data,

SIMPLE generates realistic isotropic volumes, improving upon traditional through-plane slice enhancements. Our method’s flexibility allows it to be extended across various contrast types and clinical acquisition methods.

Our experimental results demonstrate that SIMPLE outperforms state-of-the-art methods both quantitatively, as measured by KID, FID, and IS, and semi-quantitatively, through evaluations by radiologists. The generated isotropic volumes facilitate more accurate volumetric analysis and 3D reconstructions, indicating significant potential for enhancing clinical diagnostic capabilities. Future work should explore further optimizations and applications of our approach to other imaging modalities and conditions.

References

- [1] Isaac Bankman. *Handbook of medical image processing and analysis*. Elsevier, 2008. 1
- [2] Shane Barratt and Rishi Sharma. A note on the inception score. *arXiv preprint arXiv:1801.01973*, 2018. 7
- [3] Özgün Çiçek, Ahmed Abdulkadir, Soeren S Lienkamp, Thomas Brox, and Olaf Ronneberger. 3d u-net: learning dense volumetric segmentation from sparse annotation. In *Medical Image Computing and Computer-Assisted Intervention-MICCAI 2016: 19th International Conference, Athens, Greece, October 17-21, 2016, Proceedings, Part II 19*, pages 424–432. Springer, 2016. 5
- [4] Hreedi Dev, Chenglin Zhu, Arman Sharbatdaran, Syed I Raza, Sophie J Wang, Dominick J Romano, Akshay Goel, Kurt Teichman, Mina C Moghadam, George Shih, et al. Effect of averaging measurements from multiple mri pulse sequences on kidney volume reproducibility in autosomal dominant polycystic kidney disease. *Journal of Magnetic Resonance Imaging*, 58(4):1153–1160, 2023. 1
- [5] Henrique Donato, Manuela França, Isabel Candelária, and Filipe Caseiro-Alves. Liver mri: from basic protocol to advanced techniques. *European journal of radiology*, 93:30–39, 2017. 1
- [6] Wei Fang, Yuxing Tang, Heng Guo, Mingze Yuan, Tony CW Mok, Ke Yan, Jiawen Yao, Xin Chen, Zaiyi Liu, Le Lu, et al. Cycleinr: Cycle implicit neural representation for arbitrary-scale volumetric super-resolution of medical data. In *Proceedings of the IEEE/CVF Conference on Computer Vision and Pattern Recognition*, pages 11631–11641, 2024. 4
- [7] Susan T Francis, Nicholas M Selby, and Maarten W Taal. Magnetic resonance imaging to evaluate kidney structure, function, and pathology: Moving toward clinical application. *American Journal of Kidney Diseases*, 82(4):491–504, 2023. 1
- [8] Richard M Gore and Marc S Levine. *Textbook of gastrointestinal radiology*. Elsevier Health Sciences, 2021. 1
- [9] Nicholas C Gourtsoyiannis and Philip Aschoff. *Clinical MRI of the abdomen: why, how, when*. Springer, 2011. 1
- [10] Kate A Harrington, Amita Shukla-Dave, Ramesh Paudyal, and Richard KG Do. Mri of the pancreas. *Journal of Magnetic Resonance Imaging*, 53(2):347–359, 2021. 1
- [11] Phillip Isola, Jun-Yan Zhu, Tinghui Zhou, and Alexei A Efros. Image-to-image translation with conditional adversarial networks. In *Proceedings of the IEEE conference on computer vision and pattern recognition*, pages 1125–1134, 2017. 5
- [12] Yuanyuan Jia, Ali Gholipour, Zhongshi He, and Simon K Warfield. A new sparse representation framework for reconstruction of an isotropic high spatial resolution mr volume from orthogonal anisotropic resolution scans. *IEEE transactions on medical imaging*, 36(5):1182–1193, 2017. 2
- [13] Amod Jog, Aaron Carass, and Jerry L Prince. Self super-resolution for magnetic resonance images. In *Medical Image Computing and Computer-Assisted Intervention-MICCAI 2016: 19th International Conference, Athens, Greece, October 17-21, 2016, Proceedings, Part III 19*, pages 553–560. Springer, 2016. 2, 3
- [14] Armin Kanitsar, Dominik Fleischmann, Rainer Wegenkittl, Petr Felkel, and Eduard Groller. *CPR-curved planar reformation*. IEEE, 2002. 7
- [15] Sergey Kastryulin, Jamil Zakirov, Nicola Pezzotti, and Dmitry V Dylov. Image quality assessment for magnetic resonance imaging. *IEEE Access*, 11:14154–14168, 2023. 7
- [16] Zhiyang Lu, Zheng Li, Jun Wang, Jun Shi, and Dinggang Shen. Two-stage self-supervised cycle-consistency network for reconstruction of thin-slice mr images. In *Medical Image Computing and Computer Assisted Intervention-MICCAI 2021: 24th International Conference, Strasbourg, France, September 27–October 1, 2021, Proceedings, Part VI 24*, pages 3–12. Springer, 2021. 2, 3
- [17] Evan M Masutani, Naeim Bahrami, and Albert Hsiao. Deep learning single-frame and multiframe super-resolution for cardiac mri. *Radiology*, 295(3):552–561, 2020. 3
- [18] Sebastian Nowak, Narine Mesropyan, Anton Faron, Wolfgang Block, Martin Reuter, Ulrike I Attenberger, Julian A Luetkens, and Alois M Sprinkart. Detection of liver cirrhosis in standard t2-weighted mri using deep transfer learning. *European radiology*, 31(11):8807–8815, 2021. 1
- [19] Cheng Peng, S Kevin Zhou, and Rama Chellappa. Da-vsrl: domain adaptable volumetric super-resolution for medical images. In *Medical Image Computing and Computer Assisted Intervention-MICCAI 2021: 24th International Conference, Strasbourg, France, September 27–October 1, 2021, Proceedings, Part VI 24*, pages 75–85. Springer, 2021. 3
- [20] Samuel W Remedios, Shuo Han, Lianrui Zuo, Aaron Carass, Dzung L Pham, Jerry L Prince, and Blake E Dewey. Self-supervised super-resolution for anisotropic mr images with and without slice gap. In *International Workshop on Simulation and Synthesis in Medical Imaging*, pages 118–128. Springer, 2023. 2, 3, 6
- [21] Oliver Ristow, Lynne Steinbach, Gregory Sabo, Roland Krug, Markus Huber, Isabel Rauscher, Ben Ma, and Thomas M Link. Isotropic 3d fast spin-echo imaging versus standard 2d imaging at 3.0 t of the knee—image quality and diagnostic performance. *European radiology*, 19:1263–1272, 2009. 1
- [22] Jörg Sander, Bob D de Vos, and Ivana Išgum. Autoencoding low-resolution mri for semantically smooth interpolation of

anisotropic mri. *Medical image analysis*, 78:102393, 2022.

4

- [23] Karen Simonyan and Andrew Zisserman. Very deep convolutional networks for large-scale image recognition. *arXiv preprint arXiv:1409.1556*, 2014. 7
- [24] Edgardo Solano-Carrillo, Angel Bueno Rodriguez, Borja Carrillo-Perez, Yannik Steiniger, and Jannis Stoppe. Look atme: the discriminator mean entropy needs attention. In *Proceedings of the IEEE/CVF Conference on Computer Vision and Pattern Recognition*, pages 787–796, 2023. 2, 6
- [25] Xin Wang, Zhiyun Song, Yitao Zhu, Sheng Wang, Lichi Zhang, Dinggang Shen, and Qian Wang. Inter-slice super-resolution of magnetic resonance images by pre-training and self-supervised fine-tuning, 2024. 3
- [26] Haonan Zhang, Yuhang Zhang, Qing Wu, Jiangjie Wu, Zhiming Zhen, Feng Shi, Jianmin Yuan, Hongjiang Wei, Chen Liu, and Yuyao Zhang. Self-supervised arbitrary scale super-resolution framework for anisotropic mri. In *2023 IEEE 20th International Symposium on Biomedical Imaging (ISBI)*, pages 1–5. IEEE, 2023. 4
- [27] Can Zhao, Blake E Dewey, Dzung L Pham, Peter A Calabresi, Daniel S Reich, and Jerry L Prince. Smore: a self-supervised anti-aliasing and super-resolution algorithm for mri using deep learning. *IEEE transactions on medical imaging*, 40(3):805–817, 2020. 2, 3